



Mixing state of refractory black carbon in fog and haze at rural sites in winter on the North China Plain

Yuting Zhang^{1,2}, Hang Liu^{1,2}, Shandong Lei^{1,2}, Wanyun Xu³, Yu Tian^{1,2}, Weijie Yao^{1,2},
Xiaoyong Liu^{1,2,5}, Qi Liao^{1,2}, Jie Li¹, Chun Chen^{1,2}, Yele Sun^{1,2,5}, Pingqing Fu⁴, Jinyuan
5 Xin^{1,2,6}, Junji Cao⁷, Xiaole Pan¹, and Zifa Wang^{1,2,5}

¹State Key Laboratory of Atmospheric Boundary Layer Physics and Atmospheric Chemistry, Institute of
Atmospheric Physics, Chinese Academy of Sciences, Beijing 100029, China

²College of Earth and Planetary Sciences, University of Chinese Academy of Sciences, Beijing 100049,
China

10 ³State Key Laboratory of Severe Weather & Key Laboratory for Atmospheric Chemistry, Institute of
Atmospheric Composition, Chinese Academy of Meteorological Sciences, Beijing, 100081, China

⁴Institute of Surface–Earth System Science, Tianjin University, Tianjin 300072, China

⁵Center for Excellence in Regional Atmospheric Environment, Institute of Urban Environment, Chinese
Academy of Sciences, Xiamen 361021, China

15 ⁶Collaborative Innovation Center on Forecast and Evaluation of Meteorological Disasters, Nanjing
University of Information Science and Technology, Nanjing 210044, China

⁷Institute of Atmospheric Physics, Chinese Academy of Sciences, Beijing, China.

Correspondence to: Xiaole Pan (panxiaole@mail.iap.ac.cn)



20 **Abstract.** The variability of the mixing state of refractory black carbon aerosol (*r*BC) and the corresponding complicated light absorption capacity impose great uncertainty for its climate forcing assessment. In this study, field observations using a single particle soot photometer (SP2) were conducted to investigate the mixing state of *r*BC under different meteorological conditions at a rural site on the North China Plain. The results
25 showed that the hourly mass concentration of *r*BC during the observation periods was $2.6 \pm 1.5 \mu\text{g m}^{-3}$ on average with a moderate increase (3.1 ± 0.9) during fog episodes. The mass-equivalent size distribution of *r*BC exhibited an approximately lognormal distribution with a mass median diameter (MMD) of 213 nm. We found that the count median diameter (CMD) of *r*BC particles during snowfall episodes was obviously larger
30 than that before-snowfall, indicating that smaller *r*BC-containing particles were much more effectively removed by snowfall. The droplet collision and Wegener-Bergeron-Findeisen (WBF) processes are possible explanations. Based on the Mie-scattering theory simulation, the relative and absolute coating thicknesses of *r*BC-containing particles were estimated to be 1.6 and ~ 52 nm for the *r*BC core with a mass-equivalent
35 diameter (D_c) of 170 – 190 nm, respectively, indicating that the most of *r*BC-containing particles were thinly coated. Furthermore, moderate light absorption enhancement ($E_{abs} = 1.3$) and relatively low absorption cross-section ($\text{MAC} = 5.5 \text{ m}^2/\text{g}$) at 880 nm were observed at the GC site in winter compared with other typical rural sites.

The relationships between the microphysical properties of *r*BC and meteorological
40 conditions were also studied. We found that the coatings of *r*BC-containing particles increase only when both ambient RH and secondary components increase at the same time, with the thickest coating during fog events and the thinnest on clean days. And $-4 \sim 0$ °C may be the most suitable temperature range for coating formation of *r*BC in this study. The sulfate formation from aqueous-phases reactions may have a limited
45 contribution to E_{abs} under high RH conditions ($\text{RH} > 80\%$). The enhancement of E_{abs} of *r*BC-containing particles was strongly related to an increase in the mass fraction of nitrate instead of organics at appropriate temperature conditions.

Keywords: Refractory black carbon; Mixing state; Aging process; Snowfall



50 **1 Introduction**

As an absorbing aerosol produced by incomplete combustion, black carbon plays a leading role in the absorption of shortwave solar radiation, and changes atmospheric thermodynamics through the heating effect. Black carbon is an important factor leading to highly uncertain climate warming (Bond et al., 2013; Moffet and Prather, 2009). Black carbon aerosols enhance haze pollution by absorbing solar radiation to change the meteorological characteristics of the planetary boundary layer (PBL) (Ding et al., 2016). Freshly discharged black carbon is hydrophobic and becomes hydrophilic when mixed with hydrophilic material during aging, acting as cloud condensation nuclei (Sarangi et al., 2019; Twomey, 1974) and increasing the cloud drop number concentration (Cherian et al., 2017). Wet removal is a key factor in determining the lifetime of black carbon (BC) aerosols in the atmosphere, which determines their vertical and horizontal distribution, local and regional diffusion, and direct, semidirect and indirect radiative forcing effects (Liu et al., 2013).

The burning of fossil fuels such as coal and oil and the burning of biomass in agricultural production caused by human activities are the main factors leading to the increasing black carbon emissions. Using a transmission electron microscope fitted with an environmental cell (ETEM), we observed that fresh black carbon presents a loose and porous chain structure, and then in the atmosphere through condensation, coagulation, heterogeneous oxidation condensation or heterogeneous chemical reaction, *r*BC is coated by soluble material, and the coating gradually becomes thicker with increasing RH (He et al., 2015; Freney et al., 2010). The mixing state determines the morphology and optical properties of black carbon, affects its wet removal efficiency, and thus affects the atmospheric lifetime (Yu et al., 2020). The extent of *r*BC coating has been considered to be an important factor in evaluating aerosol radiative capacity (Oshima et al., 2009). It has been shown that the mixing of BC and other non-BC materials can enhance radiation absorption, which is interpreted as exhibiting a “lensing effect,” with the magnitude strongly dependent on the *r*BC coating amount (Cappa et al., 2012; Liu et al., 2015; Moffet and Prather, 2009). Generally, a thicker coating of *r*BC-containing particles with increased hygroscopic properties and the ability to act as CCN under severe pollution conditions (Ding et al., 2019a; Schwarz et al., 2008). Under high pollution and RH conditions, the adsorption efficiency of black carbon was significantly increased. Reducing the emission of



80 BC and related secondary coating precursors is an effective way to alleviate the thermal effect of BC in urban environments. However, the change in the mixing state of black carbon aerosols and their driving factors are not clear under high pollution and RH conditions.

The North China Plain is one of the BC hotspots with intensive anthropogenic emissions (Cao et al., 2006). Recently, the spatiotemporal distribution and optical properties of *r*BC and its
85 influence on climate and the environment have been reported (Zhao et al., 2020; Ding et al., 2019a; Liu et al., 2020b). However, observations of the mixing state of black carbon under different meteorological conditions are still insufficient. SP2 with high resolution and high precision has significant advantages in estimating the mixing state of black carbon. In recent years, an increasing number of observations have used SP2 to observe the mixing state of black
90 carbon in China (Wang et al., 2014; Gong et al., 2016; Liu et al., 2020b; Pan et al., 2017). Most studies have focused on the mixing state of BC on severe haze days because of the presence of large amounts of particulate matter and gaseous precursors in the atmosphere. Studies have focused on the chemical mechanisms such as condensation, coagulation, and heterogeneous oxidation for coating formation (He et al., 2015; Bond et al., 2013), while the connection
95 between meteorological factors and coatings is relatively rare. Previous studies have shown that wind speed and variation in the planetary boundary layer (PBL) can influence the concentration of BC (Talukdar et al., 2019) and that relative humidity (RH) affects the morphology and hygroscopic growth of *r*BC-containing particles (Laborde et al., 2013; Freney et al., 2010). Meteorological fields may have an impact on the mixing state of *r*BC.

100 In this study, SP2 was deployed at a moderately polluted rural site on the North China Plain in winter to characterize the size distribution and mixing state of *r*BC. This work is unique due to the largely different meteorological conditions during the campaign. The differences in *r*BC particle size under different meteorological conditions are illustrated, and the main factors influencing the *r*BC mixing state are discussed. The results of this paper were exhibited in the
105 following sequence: (1) the size distribution of *r*BC in different campaigns; (2) the relative, absolute coating thickness and optical properties of *r*BC-containing particles and its influencing factors; and (3) the relationship of the aging process of *r*BC with meteorological conditions such as RH, temperature and pollution conditions.

2 Observations



110 **2.1. Site description and measurements**

The observation of refractory BC (*r*BC) particles was performed from December 7th, 2019 to January 1st, 2020, in an air-conditioned container located in a farmland of the Gucheng (GC, latitude:39°7.8'N; longitude:115°48'E) site in Dingxing County, Hebei Province, China, which is part of the China Atmosphere Watch Network (CAWNET) operated by the Chinese Meteorological Administration (CMA). As shown in Fig.S1(a), the observation station is located ~120 kilometers southwest of Beijing, adjacent to National Highway 107 (G107) and the Beijing–Hong Kong–Macau Expressway (G4). This result indicates that the sampling site was affected by traffic emissions sources, which is a feature compared to other typical rural sites mainly affected by biomass burning sources at home and abroad. A single particle soot photometer (SP2, Droplet Measurement Technologies Inc. USA) was used to measure *r*BC and HR–AMS was used to measure the nonrefractory submicron aerosol species (NR–PM1).

120 **2.2 SP2 data analysis**

2.2.1 Instrument and calibration

The measurement of the size distribution and mixing state of individual *r*BC-containing particles in GC was characterized using an SP2. The aerosol sampling inlet was placed on a lift tower 3.5 m above the ground, and ambient air entered the container through a 1/2 in. soft black carbon tube. The SP2 was operated at a sampling flow rate of 100 vcm. There was a continuous intracavity Nd:YAG laser beam (1064 nm, TEM00 mode) in the SP2 measurement chamber. SP2 used particle identification by laser-induced incandescence technology to observe and identify *r*BC (Stephens et al., 2003; Schwarz et al., 2006). All particles scatter light, but only when they contain highly absorbent and refractory components, such as *r*BC, they absorb the laser radiation and are heated to their boiling point temperature before emitting blackbody radiation (Liu et al., 2010; Moteki and Kondo, 2007). When particles cross the laser, particles' composition and size can be determined by detecting the incandescence signal when particles evaporated and the elastic scattering signal of particles. The detection of the incandescence signal can provide information on the boiling point temperature of incandescent particles and determine the particle composition. If only the scattering signal was detected, it was proven that the particles do not contain *r*BC and are purely scattering particles (non-*r*BC). If both the scattering signal and the incandescence signal were recorded, it was an *r*BC-containing particle.



140 In general, *r*BC-containing particles need more time to evaporate the nonrefractory matter
before reaching their boiling point temperature. Therefore, there was a lag time (Δt) for the
peak of the incandescence signal and the scattering signal, which can be used to qualitatively
study the mixing state of *r*BC-containing particles. For SP2, the detectable size range of the
scattering signal was 200–400 nm diameter. Assuming a black carbon density of 1.8 g/cm³ and
145 an ideally spherical structure, the mass equivalent diameter of black carbon detected by the
incandescence signal is 70 – 500 nm.

Prior to the observation field campaign, the scattering and incandescence signals of SP2 were
calibrated in the laboratory. Aquadag aerosols (Lot #9627, Acheson Inc., USA) were used to
calibrate the incandescence signal. We used an atomizer (model 3072, TSI Inc, USA) and a
150 diffusion dryer to prepare monodispersed Aquadag aerosols, which were selected by
mobility diameter using a differential mobility analyzer (DMA; Model 3081, TSI Inc., 150
USA). The calibration coefficient values for broadband high gain (BBHG) and broadband
low gain (BBLG) of incandescence signals are shown in Fig. S2. We corrected the
incandescence signal for ambient *r*BC with a scaling factor of 0.75, because the SP2 is more
155 sensitive to Aquadag than diesel emission *r*BC in the same mass range (Laborde et al., 2012;
Baumgardner et al., 2012). The scattering signal was calibrated using polystyrene latex
spheres (PSL, Nanosphere Size Standards, Duke Scientific Corp., USA). In addition to
the above instruments, a condensation particle counter (CPC, model 3775, TSI Inc., USA)
was adopted to measure the number concentration of particles to compare with SP2.

160 2.2.2 Shell–core calculation

A single particle *r*BC mass was obtained by the incandescence signal. We usually refer to the
mass equivalent diameter converted by the *r*BC mass ($\rho = 1.8 \text{ g/cm}^3$ for ambient BC) as the *r*BC
core diameter (D_c), which is the diameter of a void-free, spherical structure, as expressed in
Eq. (1):

$$165 \quad D_c = \sqrt[3]{\frac{6 \cdot M_{rBC}}{\pi \cdot \rho_{rBC}}}, \quad (1)$$

Information about the scattering signal of *r*BC-containing particles detected by SP2 is distorted,
because when individual *r*BC particles passed through the laser beam, they absorb laser energy
and are heated up to ~4000 K, resulting in mass loss of a single *r*BC particle directly. Thus, the



methodology of leading edge only (LEO) fitting is adopted to characterize the original
170 scattering properties and coating thickness of *r*BC-containing particles. The scattering signal
of purely scattering particles is Gaussian, as detected by SP2. In this method, the Gaussian
fitting of the original scattering signal is reconstructed from the leading edge of the scattering
signal (before the volatilization of particles) of *r*BC-containing particles (Gao et al., 2007). In
this study, *r*BC-containing particles are assumed to be shell-core structures. The optical
175 diameter of *r*BC-containing particles or coated diameter (D_p) is calculated by Mie table
calculations. Using a core refractive index $n_c = 2.26 + 1.26i$ and a coating refractive index
 $n_s = 1.48 + 0i$, we input the LEO fitted scattering signal and *r*BC core size into Mie calculations
(Taylor et al., 2015). Further, the relative coating thickness (RCT), namely, the shell / core ratio
and absolute coating thickness (ACT) of an *r*BC-containing particle are calculated as D_p/D_c
180 and $(D_p - D_c)/2$, respectively.

2.2.3 Calculation of *r*BC optical properties

The ensemble effect of light absorption by *r*BC-containing particles is calculated at 880 nm,
because the optical properties of *r*BC-containing particles at this wavelength are hardly affected
by brown carbon (BrC). Based on the size information of *r*BC-containing particles (i.e., D_c and
185 D_p) obtained by SP2 observation, optical parameters such as the mass absorption cross-section
(MAC), absorption enhancement (E_{abs}) and absorption coefficient (σ_{abs}) of *r*BC-containing
particles can be obtained based on Mie scattering theory. The refractive index of the *r*BC core
was $2.26 + 1.26i$ (Bond and Bergstrom, 2006), and the refractive index of $1.48 + 0i$, was used
for coatings in the Mie calculation assuming *r*BC-containing particles is a core-shell model. In
190 addition to the absorption of light by the *r*BC core, coating materials on the surface of *r*BC can
attract more light to the *r*BC core, which called lensing effect, enhancing the light absorption
of *r*BC. The E_{abs} can be used to quantify the theoretical light absorption capability of BC-
containing particles. E_{abs} is determined by the ratio of the absorption cross-section of the whole
*r*BC-containing particle ($C_{abs,s}$) to the absorption cross-section of the bare *r*BC core ($C_{abs,c}$),
195 as shown in Eq. (2):

$$E_{abs} = \frac{C_{abs,s}}{C_{abs,c}} \quad (2)$$

MAC reflects the optical absorption characteristics of *r*BC-containing particles in unit mass



concentration. The larger the value is, the stronger the radiation absorption capacity of *r*BC-containing particles is. The mass absorption cross-section (MAC_i) of a single *r*BC-containing particle is defined as the absorption cross-section of the whole *r*BC-containing particle ($C_{abs,s}$) per unit *r*BC mass ($m_{rBC,i}$), as expressed in Eq. (3):

$$MAC_i = \frac{C_{abs,s}}{m_{rBC,i}} \quad (3)$$

The MAC in bulk for a given period is calculated as:

$$MAC = \frac{\sum_i MAC_i \times m_{rBC,i}}{\sum_i m_{rBC,i}} \quad (4)$$

The σ_{abs} of *r*BC-containing particles is calculated based on the MAC and the mass concentration (C_{rBC}) measured by SP2, as shown in Eq. (4):

$$\sigma_{abs,calculated} = MAC \times C_{rBC} \quad (5)$$

Previous studies have shown that the light absorption of *r*BC-containing particles is related to their morphology (Liu et al., 2017; Liu et al., 2020b). A simple core-shell model, used in Mie theory to calculate optical properties, causes uncertainty due to the lack of observation of optical size information and morphology.

2.3 Dispersion and trajectory analysis

The HYSPLIT (Hybrid Single-Particle Lagrangian Integrated Trajectory) model developed by NCEP (National Center for Environmental Prediction) and NCAR (National Center for Atmospheric Research) was used to simulate the air footprint area during the observation of the sampling site, which was based on the Lagrangian transport model (https://ready.arl.noaa.gov/HYSPLIT_traj.php, last access: February 28th, 2020) (Cohen et al., 2015). The dataset provided for HYSPLIT is the global reanalysis data in GDAS format (<ftp://arlftp.arlhq.noaa.gov/pub/archives/gdas1>, last access: February 26th, 2020). It produces meteorological data four times a day, namely, at 00:00, 06:00, 12:00 and 18:00 UTC, and the horizontal resolution is 2.5°×2.5°. The vertical direction has 17 levels, ranging from the ground surface to 10 hPa. Meteorological parameters including wind, temperature, humidity, potential height and ground precipitation are also provided. During the simulation, the trajectory ensemble option starts multiple trajectories from the first selected starting location. Each member of the trajectory ensemble is calculated by offsetting the meteorological data by a fixed grid factor (one meteorological grid point in the horizontal direction and 0.01σ units in the



vertical direction). Air samples were released at 150 m above ground level from the GC site, and the simulation time of the backward trajectory was 5 days.

230 3 Results and Discussion

3.1 Overview of the field observation

3.1.1 Meteorology

The field campaign was performed from December 8th to 31st 2019. During the observation period, the site was affected by the winter monsoon with a prevailing northwesterly wind (Fig. S1(b)). The meteorological conditions and the concentration of aerosol particles during the sampling period are shown in Fig. 1. The average ($\pm 1\sigma$) wind speed was $1.2 (\pm 1) \text{ m s}^{-1}$, with the highest value up to 5.9 m s^{-1} . According to the wind rose diagram, the northwest wind and the southwest wind prevailed during the observation, and the wind speed reached a maximum in the southwest direction during the whole sampling period according to the wind rose diagram (Fig.S1(c)). The relative humidity (RH) during the entire period was relatively high, with an average ($\pm 1\sigma$) of $66 (\pm 25) \%$. There were fog events and snowfall during the observation period. The period when the RH reached 100% between December 7th and 11th was defined as the fog event, and the higher RH was conducive to the condensation of hydrophilic substances on the *r*BC surface thus increasing the coating thickness and enhancing the E_{abs} of *r*BC-containing particles. Snowfall occurred at 19:00 on December 15th, and the RH began to increase before the snowfall, which was favorable for the mixing of hydrophilic substances with *r*BC. In addition, snowfall is also a method of wet removal of *r*BC-containing particles. It was of great significance to study the mixing state and removal of *r*BC-containing particles during fog and snow events to improve the model's simulation.

250 3.1.2 Mass concentration of *r*BC

The number concentrations of *r*BC and purely scattering particles showed similar variation trends. The average ($\pm 1\sigma$) number concentration of *r*BC and purely scattering particles were $650 (\pm 368)$ and $1184 (\pm 560) \# \text{ cm}^{-3}$, respectively. The mass concentration of *r*BC in the ambient environment was $2.6 (\pm 1.5) \mu\text{g m}^{-3}$, which was much lower than the observations in the winter of 2016 and 2018 at the urban site in Beijing. Liu et al., (2019) reported that the mass



concentration of *r*BC in winter 2016 in Beijing was $6.4 \mu\text{g m}^{-3}$ due to the strict air pollution control on coal combustion and biomass burning (Ji et al., 2017) Xie et al. (2020) found a decrease in mass concentration ($3.2 \mu\text{g m}^{-3}$) in winter 2018. A similar urban–high and rural–low pattern was also found in Shenzhen, and the average mass loading of *r*BC in rural areas
260 ($2.6 \mu\text{g m}^{-3}$) in autumn was much lower than that in urban areas ($6 \mu\text{g m}^{-3}$) (Huang et al., 2012). One possible explanation was that rural sites have lower traffic emissions than urban sites, open biomass burning has been strictly controlled in recent years, and the project of changing fuel from coal to natural gas has been well implemented at least in NCP (Huang et al., 2006; Ji et al., 2017).

265 Based on the meteorological conditions and concentrations of the total particles, six observation periods were chosen, as denoted in Fig. 1a: EP1 (December 7th 17:40 – December 11th 09:00), EP2 (December 12nd 19:00 – December 14th 00:00), EP3 (December 15th 00:00 – December 17th 00:00), EP4 (December 21st 00:00 – December 26th 00:00), EP5 (December 27th 00:00 – December 29th 20:00) and EP6 (December 30th 00:00 – December 31st 00:00). The periods with
270 RH = 100% during EP1 were defined as the fog period. The average RH was 96% and the average *r*BC mass concentration was $3.6 (\pm 1.4) \mu\text{g m}^{-3}$ during EP1. During EP3, there was snow from December 15th 19:00 to December 16th 13:00. Therefore, during EP3, the discussion is divided into before–snow, snow and after–snow. In the other four periods, EP6 was the clean period with an average *r*BC mass concentration of $0.5 (\pm 0.3) \mu\text{g m}^{-3}$, while EP2, EP4 and EP5
275 represented polluted periods with average *r*BC mass concentration of $3.4 (\pm 1.4)$, $1.2 (\pm 1.2)$ and $3.4 (\pm 1.3) \mu\text{g m}^{-3}$, respectively. The variables related to *r*BC and the meteorological conditions in the selected different periods are shown in Table S1. The Hysplit model was used to analyze the origin of the air masses during the different periods. As shown in Fig.2a–f, the air masses over GC mainly came from the northwest and northeast directions during the clean
280 period, and the wind speed was relatively high. During the pollution period, the air masses mainly came from the southwest and south directions and local areas. During the period of EP1 and EP3 with high RH, part of the air mass originated from the eastern Bohai Sea direction.

3.2 Size distribution of *r*BC



The time series of the mass size distribution of *r*BC during the whole experimental period was
285 stable with a modal size peaking at approximately 200nm (Fig. S3). The *r*BC-containing
particles measured by SP2 at the GC site mainly were distributed in the range of 70–400 nm
and the *r*BC mass was concentrated at 100 – 400 nm. $dM / d\log D_c$ showed an apparent diurnal
trend. The peak period of diurnal variation was between 20:00 and 09:00 LST, while low diurnal
variation occurred in the afternoon. This pattern was determined by the dual effects of diurnal
290 variation in the boundary layer and local *r*BC emissions. To better study $dM / d\log D_c$, the mass
median diameter (MMD) was used to represent the characteristics of $dM / d\log D_c$ for detailed
discussion.

Field measurements of the size of *r*BC around the world are summarized in Table 1. The size
distribution as a function of *r*BC core mass equivalent diameter (D_c) measured by SP2 is shown
295 in Fig. 3. During the whole experiment, the mass size distribution followed the lognormal
distribution and peaked at 213 nm (MMD) (Fig. 3a). As shown in Table 1, the MMD of *r*BC at
the GC site in winter was slightly smaller than the value (222 nm) observed in rural areas in
Shenzhen in November (Huang et al., 2012) and consistent with the biomass burning emission
observed in Texas (MMD = 210 nm) (Schwarz et al., 2008). However, the *r*BC emitted by
300 biomass burning in the laboratory was larger (189 nm) (Pan et al., 2017). In addition, this mode
was identical to the *r*BC mode observed in the aged continental air mass during a Paris study
(Laborde et al., 2013). In comparison with most studies in urban areas, we found that the MMD
of *r*BC in urban areas was smaller than that in our study (Huang et al., 2012; Gong et al., 2016;
Liu et al., 2019; Lan et al., 2013; Liu et al., 2020b; Schwarz et al., 2008). Laborde et al. (2013)
305 found that MMD was significantly related to the source of *r*BC-containing particle emissions.
Pan et al. (2017) showed that the MMD of *r*BC was also determined by combustion conditions
and burning materials in a laboratory study. Many studies have indicated that the MMD of *r*BC
from traffic emissions was smaller than that from biomass burning, coal combustion and aged
air masses (Laborde et al., 2013; Schwarz et al., 2008). According to previous studies, MMD
310 presented a trend of small size in summer large size in winter, small size in urban areas and
large size in rural areas (Liu et al., 2019; Liu et al., 2020b; Huang et al., 2012; Kondo et al.,
2016; Wu et al., 2021). The dense traffic arteries in urban areas and large amount of traffic



emissions may be the reason that MMD in urban areas is smaller than that in rural areas (Huang et al., 2006; Laborde et al., 2013; Schwarz et al., 2008). The different trends of MMD in seasons and spaces may be because *r*BC-containing particles came from different emission sources. In addition, the MMD was higher in pollution events (i.e., EP1, EP2, EP3 and EP5). This was similar to the results of previous studies in which under the condition of a higher *r*BC mass concentration, the *r*BC core size usually increased (Liu et al., 2019). It could be that coagulation of *r*BC particles or regional transport causes changes in *r*BC-containing particle sources at higher concentrations.

The number size distribution followed the lognormal distribution and peaked at 122 nm (CMD) (Fig. 3a). Because most *r*BC particles (by number) emitted from urban areas were below the SP2 detection limit of 70 nm, the comparison of the number size distribution between urban and rural areas was meaningless (Schwarz et al., 2008). There was snowfall during the observation period, and the mass and number size distributions of the *r*BC core mass equivalent diameter (D_c) during the snow event are illustrated in Fig. 3b–c. During before–snow, snow and after–snow periods, the MMD was 213 nm, 210 nm and 206 nm, decreasing by 3.3%, and the CMD was 120 nm, 126 nm and 129 nm, an increase of 7.5% respectively. Previous studies found that wet deposition is the main mechanism for removing of *r*BC-containing particles (Taylor et al., 2014). Wet removal plays an important role in determining the size distribution of *r*BC during vertical transport in the free troposphere (Moteki et al., 2012), and rainfalls, as a means of wet removal, preferentially removes large *r*BC-containing particles, resulting in a decrease in MMD after rain events (Liu et al., 2020b; Wang et al., 2018). However, this study found that the CMD of *r*BC-containing particles increased after–snowfall; that is, snow events would preferentially remove *r*BC-containing particles with smaller *r*BC core sizes. This may be because the wet removal mechanism of snow was different from that of rain, which was consistent with the finding that the *r*BC core size maintained a stable growth trend from 200 to 260 nm during snowfall that lasted for more than 8 hr in an observation (Ding et al., 2019b). Although the CMD increased significantly, the effect of removing a large amount of *r*BC with a small core size was small on the MMD because the large mass of *r*BC had a greater weight for the MMD. The slight decrease in MMD may be a result of snowfall, as wet removal is also



similar to rain, and can remove *r*BC with a large core size. In addition, the droplet collision and Wegener–Bergeron–Findeisen (WBF) processes may be the mechanism for extremely high removal of *r*BC with a small core size during snowfall, unlike rains (Liu et al., 2020a; 345 Ding et al., 2019b).

3.3 Mixing state of *r*BC-containing particles under different conditions

3.3.1 Coating thickness of *r*BC-containing particles

Figure 4 provides the temporal variation of ACT, RCT and CMD of *r*BC-containing particles during the entire period. The relative coating thickness (RCT) and absolute coating thickness (ACT) of *r*BC-containing particles were calculated by the LEO fitting 350 method, see Sect. 2.2.2 for details. Herein, *r*BC cores with $D_c = 180 \pm 10$ nm and $D_c = 190 \pm 10$ nm were selected because the low scattering signal of small *r*BC is easily influenced by signal noise. The average RCT ($\pm 1\sigma$) ($D_c@70\text{--}500\text{nm}$) was 2.0 (± 0.3), RCT ($\pm 1\sigma$) ($D_c@170\text{--}190\text{nm}$) was 1.6 (± 0.2), RCT ($\pm 1\sigma$) ($D_c@190\text{--}210\text{nm}$) was 1.5 355 (± 0.2), ACT ($\pm 1\sigma$) ($D_c@70\text{--}500\text{nm}$) was 57.8 (± 17.0) nm, ACT ($\pm 1\sigma$) ($D_c@170\text{--}190\text{nm}$) was 52.4 (± 21.8) nm, and ACT ($\pm 1\sigma$) ($D_c@190\text{--}210\text{nm}$) was 54.2 (± 20.4) nm. As shown in Table 1, the RCT ($D_c@190\text{--}210\text{nm}$) of GC site was consistent with the RCT (1.2–1.4) with $D_c = 200$ nm of *r*BC-containing particles emitted from biomass burning through laboratory research (Pan et al., 2017), but was larger than the value (RCT ($@D_c = 180$ 360 nm) = 1.2) during the summer in Beijing, which was mainly influenced by traffic emissions (Liu et al., 2020b). In the meantime, the RCT (2.0) with an *r*BC core size of 70–500 nm at the GC site was slightly larger than that in Beijing summer 2017 (~1.4) and smaller than that in Beijing winter 2016 (~2.5) (Liu et al., 2019). The ACT ($D_c@190\text{--}210\text{nm}$) at the GC site was smaller than that at Texas (65 nm), which was 365 affected by biomass burning. The different sources and aging processes of *r*BC-containing particles affect the coatings. Laborde et al. (2013) reported that *r*BC-containing particles emitted by traffic are essentially uncoated with median coating thickness of 2 ± 10 nm at a core size of 180–220 nm, the median ACT of *r*BC-containing particles emitted by biomass burning was approximately 20–40 nm, and the median ACT 370 of *r*BC-containing particles in continental aged air masses reached ~80 nm.



In addition, we compared the coating thickness of *r*BC-containing particles during 6 different periods. As shown in Table S1, the average RCT and ACT ($\pm 1\sigma$) ($D_c@170$ – 190 nm) were $2.0 (\pm 0.3)$ and $92.7 (\pm 23.8)$ nm, respectively, during the fog event, which were the highest values during the whole observation period. According to Fig. 7, the ambient mass concentrations of NR-PM1 were almost the same during the fog, after-snow and EP4 periods. The RH during these 3 periods was different, where the RH during the fog event was highest (RH=100%), and the RH during EP2 was lowest (RH~81%). This indicates that a high RH significantly affected on the formation of coatings under the same concentration of pollutants in the atmosphere. Fig. 5a and Fig. S4a show the RCT and ACT as a function of the *r*BC core diameter during the fog event, respectively. In these 2D images, the results of a smaller D_c (<110 nm) were meaningless due to a failed LEO fitting or the measured particle scattering signal falling outside of the Mie predictable range (Liu et al., 2014). Therefore, we only focused on the part of the $D_c > 110$ nm. The coating thickness of *r*BC-containing particles exhibited a bimodal distribution, and *r*BC-containing particles in the first peak usually had an RCT (ACT) value of 1.0 (0 nm), and the second peak had an RCT (ACT) value of ~ 1.8 (~ 70 nm) during fog events. More than 30% of the *r*BC-containing particles had an RCT of 1.5–2.2 and more than 50% of the *r*BC-containing particles had an ACT of ~ 50 nm. During the before-snow, snow and after-snow periods, the average RCTs (ACTs) ($\pm 1\sigma$) ($D_c@170$ – 190 nm) were $1.4 (\pm 0.1)$ ($39.9 (\pm 43.6)$ nm), $1.5 (\pm 0.1)$ ($46.9 (\pm 4.5)$ nm) and $1.7 (\pm 0.1)$ ($61.3 (\pm 4.7)$ nm), respectively. Fig. 5b–d and Fig. S4b–d show the RCT and ACT as a function of the *r*BC core diameter during before-snow, snow and after-snow events. The coating thickness of *r*BC-containing particles exhibited a unimodal distribution during before-snow, snow and after-snow events, with peak of RCT (ACT) values of 1.1 (15 nm), 1.2 (15 nm) and 1.2 (25 nm). From the before-snow to after-snow period, the coating thickness of *r*BC-containing particles increased gradually. We observed an increase in the secondary inorganic components and a decrease in the organic compounds in the concentration and fraction in the ambient atmosphere (Fig. 7), indicating that the coating thickness of *r*BC was intrinsically affected by the types of pollutants.



The RCT and ACT as a function of an uncoated *r*BC core diameter in pollution and clean
400 periods are shown in Fig. 6 and Fig. S5. During the pollution events (i.e., EP2 and EP5),
the *r*BC mass concentrations were almost the same, while the ambient RH during EP5
was larger than that during EP2. The coating thickness of *r*BC during EP5 with ACT (\pm
1 σ) ($D_c@170-190\text{nm}$) 48.9 (\pm 14.1) nm was larger than that during EP2 with ACT (\pm 1 σ)
($D_c@170-190\text{nm}$) 42.3 (\pm 9.4) nm. The *r*BC mass concentration during EP4 was lower than
405 that during EP5; however, due to the higher RH and higher mass fraction of nitrate during
EP4 (Fig. 7b), the coating thickness of *r*BC-containing particles during EP4 was larger
than that during EP5. EP6 was a clean period characterized by a low *r*BC mass
concentration and low ambient RH and a relatively higher mass fraction of organics in
NR-PM1. The large fraction of uncoated *r*BC-containing particles indicated that the coating
410 processes of condensation of semi-volatile organics on *r*BC particles were insignificant.

3.3.2 Absorption enhancement of *r*BC-containing particles

The E_{abs} , σ_{abs} and MAC of *r*BC-containing particles during the whole campaign are
shown in Fig.4. The average E_{abs} and MAC at 880 nm were 1.3 and 5.5 m²/g, respectively, as
calculated by Mie theory. Comparisons of E_{abs} in various field studies are shown in Table 2. The E_{abs} at
415 the GC site we simulated was consistent with the value measured by Sun et al. with TD-PAX (Droplet
Measurement Technologies) at 870 nm (1.32 ± 0.15) (Sun et al., 2021). The E_{abs} calculated by Mie
theory is only related to the core size of *r*BC, the refraction index of *r*BC-containing particles and
the coating thickness. Therefore, it is difficult to determine the relationship between E_{abs} and aerosol
species in the environment by this method. It has been suggested out that the correlation between σ_{abs}
420 calculated by Mie theory and σ_{abs} measured by AE33 is as high as 0.98, indicating that the optical
properties of *r*BC-containing particles calculated by Mie theory can represent the actual *r*BC-
containing particles in a specific area (Zhang et al., 2018b). Therefore, we compared the differences
in E_{abs} between the GC site and other regions. A moderate E_{abs} (1.21 ± 0.09) at 870 nm was found in
California 2013 during winter which was close to the present study (Zhang et al., 2016).
425 The E_{abs} was slightly larger than the value simulated using core-shell in Beijing 2018 during summer at
550 nm (1.15) (Liu et al., 2020b). Slightly high E_{abs} values were observed in Xian (1.8 at 870 nm) (Wang
et al., 2014) and Paris (1.53 ± 0.93 at 880 nm) (Zhang et al., 2018a) which represent the more polluted



urban areas. Previous studies have found that the E_{abs} is generally higher in rural areas than in urban areas, such as Shouxian (2.3 ± 0.9 at 532 nm) (Xu et al., 2018) and Yuncheng (2.25 ± 0.55 at 678 nm) (Cui et al., 2016). In addition, we studied the absorption enhancement of rBC -containing particles during 6 different periods, and specific information is detailed in Table. S1. From the before-snow to after-snow period, the coating thickness and E_{abs} of rBC -containing particles increased gradually. During the clean period, rBC with a larger core size was mostly emitted from primary sources, and the E_{abs} close to 1. In the fog event, the coating thickness was the highest among the 6 periods, while the E_{abs} was lower. This may be because the core size (D_c) of rBC during fog events was larger, rBC with a large core size (D_c) had a lower MAC, and the addition of coatings to rBC with a large D_c did not significantly affect the final total MAC compared to rBC with a small D_c (Liu et al., 2019). Compared with other rural sites, the E_{abs} and MAC of rBC -containing particles at the GC site were low. Sun et al. (2021) found that the absorption due to the lensing effect at the GC site correlated best with chloride and less well with SIA and SOA. Chloride is mainly from coal combustion and biomass burning emissions, which means that the E_{abs} at the GC site of rBC -containing particles was dominantly affected by primary species and that the coatings formed by secondary reaction products had little effect on E_{abs} . This result was consistent with the findings observed at Fresno with similar emission sources as the GC site, where the average mixing-induced absorption enhancement of BC due to the coatings can be very small (Cappa et al., 2019).

3.4 Diurnal variation of the mixing state of rBC

Figure 8 exhibits the diurnal trend of the mixing state of rBC -containing particles. The temporal variation in rBC exhibited a clear noon-low and morning and evening-high pattern while the diurnal variation in wind speed was the opposite (Fig. S6). The mean rBC mass loading increased during the evening, with a peak ($3.5 \mu\text{g m}^{-3}$) at 20:00 LST and a minimum ($1.4 \mu\text{g m}^{-3}$) at 16:00 LST, which was later than that in Beijing (Liu et al., 2020). From the diurnal variation of wind speed (Fig. S6), it can be seen that the wind speed started to increase at approximately 9:00 LST and reached a maximum (2.2 m s^{-1}) at 13:00 LST. These two-time points corresponded to the start of rBC decline and the lowest value of rBC respectively. This diurnal variation in rBC and wind speed can be explained by the diurnal variation in the boundary layer (Simpson and McGee, 2012; Talukdar et al., 2019). In the early morning, calm



inversion conditions predominate in the boundary layer. The temperature rose, the wind speed increased to an average of over 2 m s^{-1} at midday, and the $r\text{BC}$ declined rapidly with decreased atmospheric stability and increased turbulence. After sunset, the temperature dropped sharply, due to inversion and increased emissions from heating activities, and the surface pollution of $r\text{BC}$ was enhanced. The diurnal cycle of σ_{abs} was similar that of $r\text{BC}$ mass concentration, which may be because σ_{abs} of $r\text{BC}$ depends on its concentration (Zhang et al., 2018b). The diurnal variation in MAC showed an opposite trend to the MMD, indicating that MAC with a smaller $r\text{BC}$ core size was larger. The coating thickness of freshly emitted $r\text{BC}$ -containing particles was thin but thicker through a complex aging process, indicating that the RCT (ACT) was controlled by the competing effects of the aging process and emissions. The temporal variation in RCT did not present a clear day-high and night-low pattern like Beijing during summer (Liu et al., 2020b). Three peaks of the mean RCT appeared at 0:00, 8:00 and 18:00, indicating that $r\text{BC}$ emissions increased after 0:00, 8:00 and 18:00 at the GC site, and fresh $r\text{BC}$ decreased the coating thickness. In addition, there was a significant increase in RCT from the late afternoon. The light absorption enhancement of $r\text{BC}$ also did not present a strong diurnal variation trend like Beijing during June (Xie et al., 2019). This trend was consistent with the diurnal variation trend of MAC but different from that of RCT. As shown in Fig. S7, a good correlation was found between MAC (880 nm) and E_{abs} with an R^2 of 0.75 and a weak anticorrelation was found between RCT and E_{abs} with an R^2 of 0.14. This is consistent with the results discussed in Sect 3.3.2, where the E_{abs} at the GC site was more influenced by the MAC of the $r\text{BC}$ than the coating thickness. The diurnal variation in the mass fraction of aerosol species is shown in Fig. 8d. The daily cycle of mass fractions in chloride, organics and ammonium began to decrease in the late afternoon, while nitrate increased. The two higher diurnal peak values of the mass fraction of sulfate occurred at 09:00 and 16:00 LST, and the daily variation peak of the mass fraction of nitrate occurred at 16:00 LST. This may explain the increase in RCT in the late afternoon, and an increase in the mass fraction of sulfate and nitrate in the environment may favor an increase in the coating thickness of $r\text{BC}$ -containing particles. However, the diurnal cycle of light absorption enhancement of $r\text{BC}$ presented limited dependence on the aerosol species in the environment.



3.5 The dependence of the aging degree of *r*BC-containing particles on meteorological and pollution conditions

The factors that affect the aging degree of *r*BC-containing particles include photochemical reactions, aerosol species in the atmosphere and the meteorology of the environment (Laborde et al., 2013; Saathoff et al., 2003; Schnaiter, 2005). In this study, 9 RH levels (0%–20%, 20%–30%, 30%–40%, 40%–50%, 50%–60%, 60%–70%, 70%–80%, 80%–90% and 90%–100%) were selected to investigate the RH dependence of the mixing state of *r*BC. As shown in Fig. 9, we found a strong dependence of coating thickness, E_{abs} and aerosol species on RH. The average RCT increased from ~ 1.6 to 2.3 and ACT increased from ~ 41 nm to 76 nm at the GC site (Fig. S8a) as RH increased from 0% to 100%. The average E_{abs} increased from ~ 1.2 to 1.4 as RH increased from 0% to 80% and remained almost constant after RH exceeded 80%. The RH dependence of E_{abs} was likely caused by the RCT as supported by the gradual increase in the mass concentration of secondary components as a function of RH (Fig. 9c). The growth rate of coating thickness increases after RH exceeds 70%, which may be due to the liquid phase and heterogeneous reactions of secondary coatings (Collier et al., 2018; Wu et al., 2016), as explained by the steep increases in the mass concentration of nitrate and sulfate dependency on RH in the atmosphere (Fig. 9c). In addition, the mass concentration and mass fraction of Chl at the GC site showed a similar increasing trend as E_{abs} , which may imply that primary emissions contribute more to E_{abs} than secondary components. Moreover, only the mass fraction of sulfate in the secondary components increased steeply when the RH was above 80%, which may indicate that the sulfate formed by the aqueous-phase reaction made a limited contribution to the E_{abs} .

The temperature effect on the mixing state of *r*BC-containing particles is examined in Fig. 10. A positive response of RCT, RH and mass concentration of aerosol species to temperature was observed for the temperature range of $-14 \sim 0$ °C, suggesting that this temperature range was a favorable condition for coating formation on *r*BC at the GC site. However, a further temperature increment beyond 0 °C led to a decline in the coating thickness. This can be explained by the variation trend of aerosol species in the environment with temperature. When the temperature was below 0 °C, the concentration of secondary components increased as the temperature rose,



515 which may favor the formation of coatings on *r*BC. Previous studies have found that particles' growth depends on the competition between particles and water vapor under heavy pollution conditions, and the temperature has a significant influence on condensation growth (Okuyama et al., 2007). Therefore, $-4 \sim 0$ °C may be the most conducive temperature range for water vapor to compete with particles and condense on the surface of *r*BC. Note that E_{abs} increased with
520 increasing temperature when the temperature range was below 4 °C and decreased when the temperature exceeded 4 °C, which was different from the temperature dependence on RCT. In this study, we found that the mass concentration and mass fraction of nitrate decreased after the temperature exceeded 4 °C (Fig. 10d). The evaporation of volatile components due to increased temperature could be the explanation (Sun et al., 2020). Higher temperatures facilitate the
525 transition of volatile components such as nitrates and volatile organic compounds from the solid phase to the gas phase. As shown in Fig. S6, the temperature at the GC site increased in the afternoon, and the nitrate decreased significantly at the same time, indicating that nitrate evaporated. A study in Beijing found that nitrate evaporation weakens E_{abs} (Xie et al., 2019). Another chamber study found that during the chemical aging process of *r*BC, E_{abs} was reduced
530 due to the evaporation of SOA (Metcalf et al., 2012). Temperature-dependent gas-particle partitioning also played an important role in E_{abs} .

4 Conclusions

The size distribution, coating thickness and optical properties of individual *r*BC-containing particles were measured by a single-particle soot photometer (SP2) during the period December
535 7th to December 31st, 2019 to characterize the mixing state of *r*BC-containing particles in rural areas on the North China Plain. We analyzed the mixing state and optical properties of *r*BC-containing particles in different episodes and discussed the factors affecting the aging degree of *r*BC. The MMD of *r*BC in the GC site was 213 nm which was smaller than that in other rural areas. Meteorological conditions can significantly affect the mass size distribution. Snowfall
540 preferred to remove *r*BC-containing particles with smaller core sizes due to droplet collision and Wegener-Bergeron-Findeisen processes. The average RCT (ACT) was 1.6 (52 nm) when the D_c was in the range of 170 nm ~ 190 nm, indicating a moderate coating thickness of *r*BC during the winter. The coating thickness of *r*BC-containing particles in the fog event was thicker than that in other periods due to the high RH and high concentration of secondary



545 aerosols. The ensemble-average mixing-induced E_{abs} and MAC at the GC site were smaller than those at other rural areas. The RCT ($D_c@70-500\text{nm}$) and E_{abs} did not show clear diurnal cycles with little variations in the range of $\sim 1.9-2$, and $1.3-1.4$, respectively. A good correlation was found between MAC (880 nm) and E_{abs} with an R^2 of 0.75 and a weak anticorrelation was found between RCT and E_{abs} with an R^2 of 0.14 under diurnal cycle. This may be because the optical
550 properties of rBC in the GC site were mainly influenced by primary emissions (such as coal combustion, biomass burning and traffic emission), and the absorption due to lensing effect contributes less to it.

Our results showed that the mixing state of rBC-containing particles depends on the synergistic effects of ambient RH, temperature and aerosol species due to complex chemical reactions.
555 With the increase in the mass fraction of secondary components and the decrease in the mass fraction of organic matter, the coating thickness of rBC-containing particles tended to be thicker. $RH > 70\%$, secondary components (e.g., nitrate and sulfate) generated by the liquid phase and non-homogeneous reactions favored the formation of coatings. $RH > 80\%$, the contribution of sulfate formed by the aqueous phase reaction to E_{abs} was limited. The effect of
560 temperature on the aging degree of rBC-containing particles was reflected in the temperature dependence of particle condensation growth and gas-particle partitioning. Volatile components such as nitrate and organics are sensitive to temperature. The temperature range of $-14 \sim 0 \text{ }^\circ\text{C}$ was favorable for coating thicknesses formation. Our study found that when the temperature in the rural areas of GC rises to $4 \text{ }^\circ\text{C}$, the coating thickness and E_{abs} of rBC-containing particles
565 decrease; in addition, the mass concentration and mass fraction of nitrate decrease, correspondingly. This suggests that when the temperature in rural areas rises to $4 \text{ }^\circ\text{C}$, volatile components such as nitrate move from the solid phase to the gas phase, resulting in a smaller coating thickness and E_{abs} of rBC-containing particles. Our results highlight that the aging degree of rBC in different chemical environments needs to be considered in regional climate
570 models to better evaluate the radiative forcing of rBC.



Data availability. To request the data given in this study, please contact Xiaole Pan at the Institute of Atmospheric Physics, Chinese Academy of Sciences, via email (panxiaole@mail.iap.ac.cn).

575 *Author contributions.* YZ, SL, HL, and XP designed the research. YZ, SL, HL, XP, WX, YT, WY, XL, QL, JL, CC, YS, PF, JX, JC and ZW performed the experiments. YZ, SL, HL and XP performed the data analysis. YZ, HL, XP and SL wrote the paper.

Competing interests. The authors declare that they have no conflict of interest.

580

Financial support. This research has been supported by the National Natural Science Foundation of China (grant nos. 4187072067).

References

- 585 Baumgardner, D., Popovicheva, O., Allan, J., Bernardoni, V., Cao, J., Cavalli, F., Cozic, J., Diapouli, E., Eleftheriadis, K., Genberg, P. J., Gonzalez, C., Gysel, M., John, A., Kirchstetter, T. W., Kuhlbusch, T. A. J., Laborde, M., Lack, D., Müller, T., Niessner, R., Petzold, A., Piazzalunga, A., Putaud, J. P., Schwarz, J., Sheridan, P., Subramanian, R., Swietlicki, E., Valli, G., Vecchi, R., and Viana, M.: Soot reference materials for instrument calibration and intercomparisons: a workshop summary with recommendations, Atmospheric Measurement Techniques, 5, 1869–1887, 10.5194/amt-5-1869-2012, 2012.
- 590 Bond, T. C., Doherty, S. J., Fahey, D. W., Forster, P. M., Berntsen, T., DeAngelo, B. J., Flanner, M. G., Ghan, S., Kärcher, B., Koch, D., Kinne, S., Kondo, Y., Quinn, P. K., Sarofim, M. C., Schultz, M. G., Schulz, M., Venkataraman, C., Zhang, H., Zhang, S., Bellouin, N., Guttikunda, S. K., Hopke, P. K., Jacobson, M. Z., Kaiser, J. W., Klimont, Z., Lohmann, U., Schwarz, J. P., Shindell, D., Storelvmo, T., Warren, S. G., and Zender, C. S.: Bounding the role of black carbon in the climate system: A scientific assessment, Journal of Geophysical Research: Atmospheres, 118, 5380–5552, 10.1002/jgrd.50171, 2013.
- 595 Cao, G., Zhang, X., and Zheng, F.: Inventory of black carbon and organic carbon emissions from China, Atmospheric Environment, 40, 6516–6527, 10.1016/j.atmosenv.2006.05.070, 2006.
- Cappa, C. D., Onasch, T. B., Massoli, P., Worsnop, D. R., Bates, T. S., Cross, E. S., Davidovits, P., 600 Hakala, J., Hayden, K. L., Jobson, B. T., Kolesar, K. R., Lack, D. A., Lerner, B. M., Li, S.-M., Mellon, D., Nuaaman, I., Olfert, J. S., Petaja, T., Quinn, P. K., Song, C., Subramanian, R., Williams, E. J., and Zaveri, R. A.: Radiative Absorption Enhancements Due to the Mixing State of Atmospheric Black Carbon, Science, 337, 1078–1081, 10.1126/science.1223447, 2012.
- Cappa, C. D., Zhang, X., Russell, L. M., Collier, S., Lee, A. K. Y., Chen, C.-L., Betha, R., Chen, S., Liu, J., Price, D. J., Sanchez, K. J., McMeeking, G. R., Williams, L. R., Onasch, T. B., Worsnop, D. R., Abbatt, J., and Zhang, Q.: Light Absorption by Ambient Black and Brown Carbon and its Dependence on Black Carbon Coating State for Two California, USA, Cities in Winter and Summer, Journal of Geophysical Research: Atmospheres, 124, 1550–1577, 10.1029/2018jd029501, 2019.



- Cherian, R., Quaas, J., Salzmänn, M., and Tomassini, L.: Black carbon indirect radiative effects in a climate model, *Tellus B: Chemical and Physical Meteorology*, 69, 10.1080/16000889.2017.1369342, 2017.
- Cohen, M. D., Stunder, B. J. B., Rolph, G. D., Draxler, R. R., Stein, A. F., and Ngan, F.: NOAA's HYSPLIT Atmospheric Transport and Dispersion Modeling System, *Bulletin of the American Meteorological Society*, 96, 2059–2077, 10.1175/bams-d-14-00110.1, 2015.
- Collier, S., Williams, L. R., Onasch, T. B., Cappa, C. D., Zhang, X., Russell, L. M., Chen, C.-L., Sanchez, K. J., Worsnop, D. R., and Zhang, Q.: Influence of Emissions and Aqueous Processing on Particles Containing Black Carbon in a Polluted Urban Environment: Insights From a Soot Particle–Aerosol Mass Spectrometer, *J. Geophys. Res.–Atmos.*, 123, 6648–6666, 10.1002/2017jd027851, 2018.
- Cui, X., Wang, X., Yang, L., Chen, B., Chen, J., Andersson, A., and Gustafsson, O.: Radiative absorption enhancement from coatings on black carbon aerosols, *Sci Total Environ*, 551–552, 51–56, 10.1016/j.scitotenv.2016.02.026, 2016.
- Ding, A. J., Huang, X., Nie, W., Sun, J. N., Kerminen, V. M., Petaja, T., Su, H., Cheng, Y. F., Yang, X. Q., Wang, M. H., Chi, X. G., Wang, J. P., Virkkula, A., Guo, W. D., Yuan, J., Wang, S. Y., Zhang, R. J., Wu, Y. F., Song, Y., Zhu, T., Zilitinkevich, S., Kulmala, M., and Fu, C. B.: Enhanced haze pollution by black carbon in megacities in China, *Geophysical Research Letters*, 43, 2873–2879, 10.1002/2016gl067745, 2016.
- Ding, S., Liu, D., Zhao, D., Hu, K., Tian, P., Zhou, W., Huang, M., Yang, Y., Wang, F., Sheng, J., Liu, Q., Kong, S., Cui, P., Huang, Y., He, H., Coe, H., and Ding, D.: Size-Related Physical Properties of Black Carbon in the Lower Atmosphere over Beijing and Europe, *Environ Sci Technol*, 53, 11112–11121, 10.1021/acs.est.9b03722, 2019a.
- Ding, S., Zhao, D., He, C., Huang, M., He, H., Tian, P., Liu, Q., Bi, K., Yu, C., Pitt, J., Chen, Y., Ma, X., Chen, Y., Jia, X., Kong, S., Wu, J., Hu, D., Hu, K., Ding, D., and Liu, D.: Observed Interactions Between Black Carbon and Hydrometeor During Wet Scavenging in Mixed-Phase Clouds, *Geophysical Research Letters*, 46, 8453–8463, 10.1029/2019gl083171, 2019b.
- Freney, E. J., Adachi, K., and Buseck, P. R.: Internally mixed atmospheric aerosol particles: Hygroscopic growth and light scattering, *Journal of Geophysical Research*, 115, 10.1029/2009jd013558, 2010.
- Gao, R. S., Schwarz, J. P., Kelly, K. K., Fahey, D. W., Watts, L. A., Thompson, T. L., Spackman, J. R., Slowik, J. G., Cross, E. S., Han, J. H., Davidovits, P., Onasch, T. B., and Worsnop, D. R.: A Novel Method for Estimating Light-Scattering Properties of Soot Aerosols Using a Modified Single-Particle Soot Photometer, *Aerosol Science and Technology*, 41, 125–135, 10.1080/02786820601118398, 2007.
- Gong, X., Zhang, C., Chen, H., Nizkorodov, S. A., Chen, J., and Yang, X.: Size distribution and mixing state of black carbon particles during a heavy air pollution episode in Shanghai, *Atmospheric Chemistry and Physics*, 16, 5399–5411, 10.5194/acp-16-5399-2016, 2016.
- He, C., Liou, K. N., Takano, Y., Zhang, R., Levy Zamora, M., Yang, P., Li, Q., and Leung, L. R.: Variation of the radiative properties during black carbon aging: theoretical and experimental intercomparison, *Atmospheric Chemistry and Physics*, 15, 11967–11980, 10.5194/acp-15-11967-2015, 2015.
- Huang, X.-F., Sun, T.-L., Zeng, L.-W., Yu, G.-H., and Luan, S.-J.: Black carbon aerosol characterization in a coastal city in South China using a single particle soot photometer, *Atmospheric Environment*, 51, 21–28, 10.1016/j.atmosenv.2012.01.056, 2012.
- Huang, X. F., Yu, J. Z., He, L. Y., and Hu, M.: Size distribution characteristics of elemental carbon emitted from Chinese vehicles: Results of a tunnel study and atmospheric implications, *Environ. Sci.*



- Technol., 40, 5355–5360, 10.1021/es0607281, 2006.
- Ji, D., Li, L., Pang, B., Xue, P., Wang, L., Wu, Y., Zhang, H., and Wang, Y.: Characterization of black carbon in an urban–rural fringe area of Beijing, *Environ Pollut*, 223, 524–534, 10.1016/j.envpol.2017.01.055, 2017.
- 655 Kondo, Y., Moteki, N., Oshima, N., Ohata, S., Koike, M., Shibano, Y., Takegawa, N., and Kita, K.: Effects of wet deposition on the abundance and size distribution of black carbon in East Asia, *Journal of Geophysical Research: Atmospheres*, 121, 4691–4712, 10.1002/2015jd024479, 2016.
- 660 Laborde, M., Mertes, P., Zieger, P., Dommen, J., Baltensperger, U., and Gysel, M.: Sensitivity of the Single Particle Soot Photometer to different black carbon types, *Atmospheric Measurement Techniques*, 5, 1031–1043, 10.5194/amt-5-1031-2012, 2012.
- Laborde, M., Crippa, M., Tritscher, T., Jurányi, Z., Decarlo, P. F., Temime-Roussel, B., Marchand, N., Eckhardt, S., Stohl, A., Baltensperger, U., Prévôt, A. S. H., Weingartner, E., and Gysel, M.: Black carbon physical properties and mixing state in the European megacity Paris, *Atmospheric Chemistry and Physics*, 13, 5831–5856, 10.5194/acp-13-5831-2013, 2013.
- 665 Lan, Z.-J., Huang, X.-F., Yu, K.-Y., Sun, T.-L., Zeng, L.-W., and Hu, M.: Light absorption of black carbon aerosol and its enhancement by mixing state in an urban atmosphere in South China, *Atmospheric Environment*, 69, 118–123, 10.1016/j.atmosenv.2012.12.009, 2013.
- 670 Liu, D., Flynn, M., Gysel, M., Targino, A., Crawford, I., Bower, K., Choulaton, T., Jurányi, Z., Steinbacher, M., Hüglin, C., Curtius, J., Kampus, M., Petzold, A., Weingartner, E., Baltensperger, U., and Coe, H.: Single particle characterization of black carbon aerosols at a tropospheric alpine site in Switzerland, *Atmospheric Chemistry and Physics*, 10, 7389–7407, 10.5194/acp-10-7389-2010, 2010.
- Liu, D., Allan, J., Whitehead, J., Young, D., Flynn, M., Coe, H., McFiggans, G., Fleming, Z. L., and Bandy, B.: Ambient black carbon particle hygroscopic properties controlled by mixing state and composition, *Atmospheric Chemistry and Physics*, 13, 2015–2029, 10.5194/acp-13-2015-2013, 2013.
- 675 Liu, D., Allan, J. D., Young, D. E., Coe, H., Beddows, D., Fleming, Z. L., Flynn, M. J., Gallagher, M. W., Harrison, R. M., Lee, J., Prevot, A. S. H., Taylor, J. W., Yin, J., Williams, P. I., and Zotter, P.: Size distribution, mixing state and source apportionment of black carbon aerosol in London during wintertime, *Atmospheric Chemistry and Physics*, 14, 10061–10084, 10.5194/acp-14-10061-2014, 2014.
- 680 Liu, D., Joshi, R., Wang, J., Yu, C., Allan, J. D., Coe, H., Flynn, M. J., Xie, C., Lee, J., Squires, F., Kotthaus, S., Grimmond, S., Ge, X., Sun, Y., and Fu, P.: Contrasting physical properties of black carbon in urban Beijing between winter and summer, *Atmospheric Chemistry and Physics*, 19, 6749–6769, 10.5194/acp-19-6749-2019, 2019.
- 685 Liu, D., He, C., Schwarz, J. P., and Wang, X.: Lifecycle of light-absorbing carbonaceous aerosols in the atmosphere, *npj Climate and Atmospheric Science*, 3, 10.1038/s41612-020-00145-8, 2020a.
- Liu, D. T., Whitehead, J., Alfarra, M. R., Reyes-Villegas, E., Spracklen, D. V., Reddington, C. L., Kong, S. F., Williams, P. I., Ting, Y. C., Haslett, S., Taylor, J. W., Flynn, M. J., Morgan, W. T., McFiggans, G., Coe, H., and Allan, J. D.: Black-carbon absorption enhancement in the atmosphere determined by particle mixing state, *Nature Geoscience*, 10, 184–U132, 10.1038/ngeo2901, 2017.
- 690 Liu, H., Pan, X., Liu, D., Liu, X., Chen, X., Tian, Y., Sun, Y., Fu, P., and Wang, Z.: Mixing characteristics of refractory black carbon aerosols at an urban site in Beijing, *Atmospheric Chemistry and Physics*, 20, 5771–5785, 10.5194/acp-20-5771-2020, 2020b.
- Liu, S., Aiken, A. C., Gorkowski, K., Dubey, M. K., Cappa, C. D., Williams, L. R., Herndon, S. C., Massoli, P., Fortner, E. C., Chhabra, P. S., Brooks, W. A., Onasch, T. B., Jayne, J. T., Worsnop, D. R., China, S., Sharma, N., Mazzoleni, C., Xu, L., Ng, N. L., Liu, D., Allan, J. D., Lee, J. D., Fleming, Z. L.,



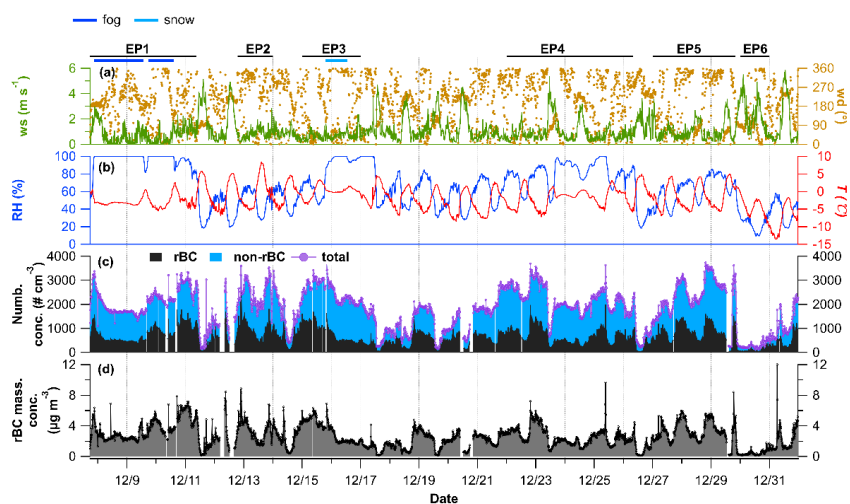
- Mohr, C., Zotter, P., Szidat, S., and Prevot, A. S. H.: Enhanced light absorption by mixed source black and brown carbon particles in UK winter, *Nat Commun*, 6, 8435, 10.1038/ncomms9435, 2015.
- Metcalf, A. R., Loza, C. L., Coggon, M. M., Craven, J. S., Jonsson, H. H., Flagan, R. C., and Seinfeld, J. H.: Secondary Organic Aerosol Coating Formation and Evaporation: Chamber Studies Using Black Carbon Seed Aerosol and the Single-Particle Soot Photometer, *Aerosol Science and Technology*, 47, 326–347, 10.1080/02786826.2012.750712, 2012.
- 700
- Moffet, R. C., and Prather, K. A.: In-situ measurements of the mixing state and optical properties of soot with implications for radiative forcing estimates, *Proceedings of the National Academy of Sciences of the United States of America*, 106, 11872–11877, 10.1073/pnas.0900040106, 2009.
- 705
- Moteki, N., and Kondo, Y.: Effects of Mixing State on Black Carbon Measurements by Laser-Induced Incandescence, *Aerosol Science and Technology*, 41, 398–417, 10.1080/02786820701199728, 2007.
- Moteki, N., Kondo, Y., Oshima, N., Takegawa, N., Koike, M., Kita, K., Matsui, H., and Kajino, M.: Size dependence of wet removal of black carbon aerosols during transport from the boundary layer to the free troposphere, *Geophysical Research Letters*, 39, 10.1029/2012gl052034, 2012.
- 710
- Okuyama, K., Kousaka, Y., and Motouchi, T.: Condensational Growth of Ultrafine Aerosol Particles in a New Particle Size Magnifier, *Aerosol Science and Technology*, 3, 353–366, 10.1080/02786828408959024, 2007.
- Oshima, N., Koike, M., Zhang, Y., Kondo, Y., Moteki, N., Takegawa, N., and Miyazaki, Y.: Aging of black carbon in outflow from anthropogenic sources using a mixing state resolved model: Model development and evaluation, *Journal of Geophysical Research*, 114, 10.1029/2008jd010680, 2009.
- 715
- Pan, X., Kanaya, Y., Taketani, F., Miyakawa, T., Inomata, S., Komazaki, Y., Tanimoto, H., Wang, Z., Uno, I., and Wang, Z.: Emission characteristics of refractory black carbon aerosols from fresh biomass burning: a perspective from laboratory experiments, *Atmospheric Chemistry and Physics*, 17, 13001–13016, 10.5194/acp-17-13001-2017, 2017.
- 720
- Saathoff, H., Naumann, K. H., Schnaiter, M., Schöck, W., Möhler, O., Schurath, U., Weingartner, E., Gysel, M., and Baltensperger, U.: Coating of soot and (NH₄)₂SO₄ particles by ozonolysis products of α -pinene, *Journal of Aerosol Science*, 34, 1297–1321, 10.1016/s0021-8502(03)00364-1, 2003.
- Sarang, B., Ramachandran, S., Rajesh, T. A., and Dhaker, V. K.: Black carbon linked aerosol hygroscopic growth: Size and mixing state are crucial, *Atmospheric Environment*, 200, 110–118, 10.1016/j.atmosenv.2018.12.001, 2019.
- 725
- Schnaiter, M.: Absorption amplification of black carbon internally mixed with secondary organic aerosol, *Journal of Geophysical Research*, 110, 10.1029/2005jd006046, 2005.
- Schwarz, J. P., Gao, R. S., Fahey, D. W., Thomson, D. S., Watts, L. A., Wilson, J. C., Reeves, J. M., Darbeheshti, M., Baumgardner, D. G., Kok, G. L., Chung, S. H., Schulz, M., Hendricks, J., Lauer, A., Karcher, B., Slowik, J. G., Rosenlof, K. H., Thompson, T. L., Langford, A. O., Loewenstein, M., and Aikin, K. C.: Single-particle measurements of midlatitude black carbon and light-scattering aerosols from the boundary layer to the lower stratosphere, *J. Geophys. Res.–Atmos.*, 111, 15, 10.1029/2006jd007076, 2006.
- 730
- Schwarz, J. P., Gao, R. S., Spackman, J. R., Watts, L. A., Thomson, D. S., Fahey, D. W., Ryerson, T. B., Peischl, J., Holloway, J. S., Trainer, M., Frost, G. J., Baynard, T., Lack, D. A., de Gouw, J. A., Warneke, C., and Del Negro, L. A.: Measurement of the mixing state, mass, and optical size of individual black carbon particles in urban and biomass burning emissions, *Geophysical Research Letters*, 35, 10.1029/2008gl033968, 2008.
- 735
- 740
- Stephens, M., Turner, N., and Sandberg, J.: Particle identification by laser-induced incandescence in a



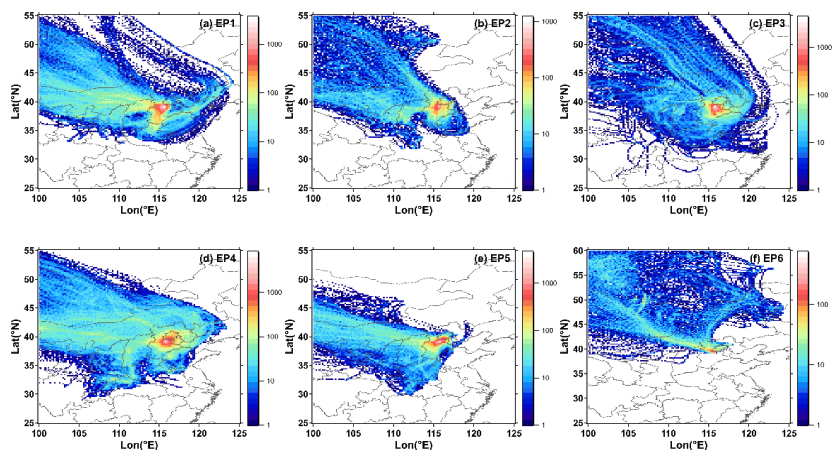
- solid-state laser cavity, *Appl. Optics*, 42, 3726–3736, 10.1364/ao.42.003726, 2003.
- Sun, J., Xie, C., Xu, W., Chen, C., Ma, N., Xu, W., Lei, L., Li, Z., He, Y., Qiu, Y., Wang, Q., Pan, X., Su, H., Cheng, Y., Wu, C., Fu, P., Wang, Z., and Sun, Y.: Light absorption of black carbon and brown carbon in winter in North China Plain: comparisons between urban and rural sites, *Science of The Total Environment*, 770, 10.1016/j.scitotenv.2020.144821, 2021.
- 745 Sun, J. Y., Wu, C., Wu, D., Cheng, C. L., Li, M., Li, L., Deng, T., Yu, J. Z., Li, Y. J., Zhou, Q. N., Liang, Y., Sun, T. L., Song, L., Cheng, P., Yang, W. D., Pei, C. L., Chen, Y. N., Cen, Y. X., Nian, H. Q., and Zhou, Z.: Amplification of black carbon light absorption induced by atmospheric aging: temporal variation at seasonal and diel scales in urban Guangzhou, *Atmospheric Chemistry and Physics*, 20, 2445–2470, 10.5194/acp-20-2445-2020, 2020.
- 750 Talukdar, S., Venkat Ratnam, M., Ravikiran, V., and Chakraborty, R.: Influence of Black Carbon Aerosol on the Atmospheric Instability, *Journal of Geophysical Research: Atmospheres*, 124, 5539–5554, 10.1029/2018jd029611, 2019.
- Taylor, J. W., Allan, J. D., Allen, G., Coe, H., Williams, P. I., Flynn, M. J., Le Breton, M., Muller, J. B. A., Percival, C. J., Oram, D., Forster, G., Lee, J. D., Rickard, A. R., Parrington, M., and Palmer, P. I.: Size-dependent wet removal of black carbon in Canadian biomass burning plumes, *Atmospheric Chemistry and Physics*, 14, 13755–13771, 10.5194/acp-14-13755-2014, 2014.
- 755 Taylor, J. W., Allan, J. D., Liu, D., Flynn, M., Weber, R., Zhang, X., Lefer, B. L., Grossberg, N., Flynn, J., and Coe, H.: Assessment of the sensitivity of core / shell parameters derived using the single-particle soot photometer to density and refractive index, *Atmospheric Measurement Techniques*, 8, 1701–1718, 10.5194/amt-8-1701-2015, 2015.
- 760 Twomey, S.: POLLUTION AND PLANETARY ALBEDO, *Atmospheric Environment*, 8, 1251–1256, 10.1016/0004-6981(74)90004-3, 1974.
- 765 Wang, Q., Huang, R. J., Cao, J., Han, Y., Wang, G., Li, G., Wang, Y., Dai, W., Zhang, R., and Zhou, Y.: Mixing State of Black Carbon Aerosol in a Heavily Polluted Urban Area of China: Implications for Light Absorption Enhancement, *Aerosol Science and Technology*, 48, 689–697, 10.1080/02786826.2014.917758, 2014.
- 770 Wang, Q., Cao, J., Han, Y., Tian, J., Zhu, C., Zhang, Y., Zhang, N., Shen, Z., Ni, H., Zhao, S., and Wu, J.: Sources and physicochemical characteristics of black carbon aerosol from the southeastern Tibetan Plateau: internal mixing enhances light absorption, *Atmospheric Chemistry and Physics*, 18, 4639–4656, 10.5194/acp-18-4639-2018, 2018.
- 775 Wu, Y., Zhang, R., Tian, P., Tao, J., Hsu, S. C., Yan, P., Wang, Q., Cao, J., Zhang, X., and Xia, X.: Effect of ambient humidity on the light absorption amplification of black carbon in Beijing during January 2013, *Atmospheric Environment*, 124, 217–223, 10.1016/j.atmosenv.2015.04.041, 2016.
- 780 Wu, Y., Xia, Y., Zhou, C., Tian, P., Tao, J., Huang, R. J., Liu, D., Wang, X., Xia, X., Han, Z., and Zhang, R.: Effect of source variation on the size and mixing state of black carbon aerosol in urban Beijing from 2013 to 2019: Implication on light absorption, *Environ Pollut*, 270, 116089, 10.1016/j.envpol.2020.116089, 2021.
- Xie, C. H., Xu, W. Q., Wan, J. F., Liu, D. T., Ge, X. L., Zhang, Q., Wang, Q., Du, W., Zhao, J., Zhou, W., Li, J., Fu, P. Q., Wang, Z. F., Worsnop, D. L., and Sun, Y. L.: Light absorption enhancement of black carbon in urban Beijing in summer, *Atmospheric Environment*, 213, 499–504, 10.1016/j.atmosenv.2019.06.041, 2019.
- Xu, X., Zhao, W., Qian, X., Wang, S., Fang, B., Zhang, Q., Zhang, W., Venables, D. S., Chen, W., Huang, Y., Deng, X., Wu, B., Lin, X., Zhao, S., and Tong, Y.: The influence of photochemical aging on light



- 785 absorption of atmospheric black carbon and aerosol single-scattering albedo, *Atmospheric Chemistry and Physics*, 18, 16829–16844, 10.5194/acp-18-16829-2018, 2018.
- Yu, C., Liu, D., Broda, K., Joshi, R., Olfert, J., Sun, Y., Fu, P., Coe, H., and Allan, J. D.: Characterising mass-resolved mixing state of black carbon in Beijing using a morphology-independent measurement method, *Atmospheric Chemistry and Physics*, 20, 3645–3661, 10.5194/acp-20-3645-2020, 2020.
- 790 Zhang, X., Kim, H., Parworth, C. L., Young, D. E., Zhang, Q., Metcalf, A. R., and Cappa, C. D.: Optical Properties of Wintertime Aerosols from Residential Wood Burning in Fresno, CA: Results from DISCOVER-AQ 2013, *Environ. Sci. Technol.*, 50, 1681–1690, 10.1021/acs.est.5b04134, 2016.
- Zhang, Y., Favez, O., Canonaco, F., Liu, D., Močnik, G., Amodeo, T., Sciare, J., Prévôt, A. S. H., Gros, V., and Albinet, A.: Evidence of major secondary organic aerosol contribution to lensing effect black carbon absorption enhancement, *npj Climate and Atmospheric Science*, 1, 10.1038/s41612-018-0056-2, 2018a.
- 795 Zhang, Y., Zhang, Q., Cheng, Y., Su, H., Li, H., Li, M., Zhang, X., Ding, A., and He, K.: Amplification of light absorption of black carbon associated with air pollution, *Atmospheric Chemistry and Physics*, 18, 9879–9896, 10.5194/acp-18-9879-2018, 2018b.
- 800 Zhao, D., Liu, D., Yu, C., Tian, P., Hu, D., Zhou, W., Ding, S., Hu, K., Sun, Z., Huang, M., Huang, Y., Yang, Y., Wang, F., Sheng, J., Liu, Q., Kong, S., Li, X., He, H., and Ding, D.: Vertical evolution of black carbon characteristics and heating rate during a haze event in Beijing winter, *Sci Total Environ*, 709, 136251, 10.1016/j.scitotenv.2019.136251, 2020.



805 **Figure 1:** Time series of (a) wind speed (ws) and wind direction (wd), (b) relative humidity (RH) and ambient temperature (T), (c) number concentration of rBC-containing particles, purely scattering particles and total particles measured by SP2 in GC and (d) rBC mass loading.



810 **Figure 2:** The backward trajectories from which the air mass over GC originated in varying periods.

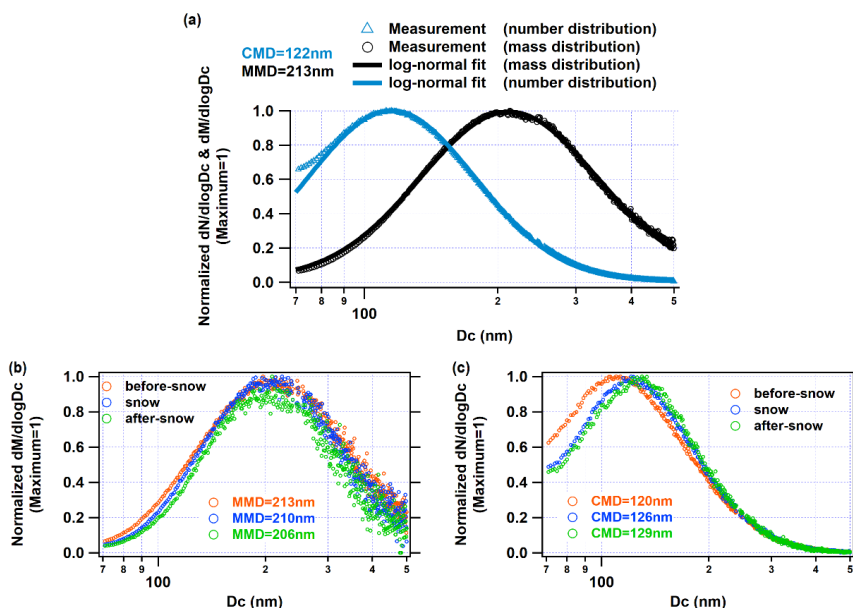
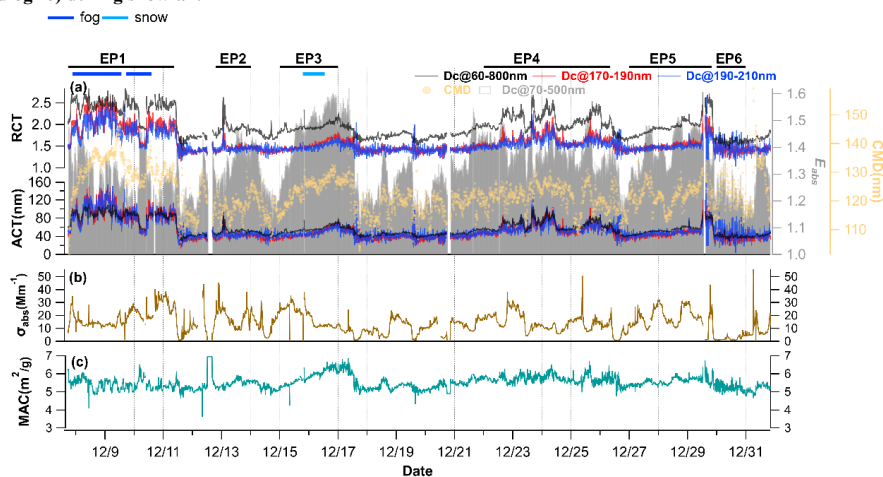


Figure 3: (a) Number and mass size distribution ($dN / d\log D_c$ and $dM / d\log D_c$) of *rBC* core during the whole campaign. (b) Mass size distribution ($dM / d\log D_c$) during snowfall and (c) number size distribution ($dN / d\log D_c$) during snowfall.



815

Figure 4: (a) Time series of the relative and absolute coating thicknesses of *rBC*-containing particles within the Dc range of 170–190 nm, 190–210 nm and the entire SP2 detectable Dc range (70–500 nm). The gray bars denote the absorption enhancement (E_{abs}) of *rBC* within the Dc range of the entire SP2 detectable Dc range (70–500 nm). The light yellow circles denote the size of the *rBC* core. Time series of the (b) absorption coefficient (σ_{abs}) and (c) mass absorption cross-section (MAC).

820



825

Table 1. Brief summary of some of the experiments on the size and mixing state of rBC-containing particles.

rBC source	Location	Time	CMD (nm)	MMD (nm)	RCT	ACT (nm)	Reference
Urban emission (UE)	Beijing, China	Jun (Summer)		171	1.2(@Dc=180 nm)		Liu et al. (2020)
	Shenzhen, China	Aug-Sep (Fall)		180*			Lan et al. (2013)
	Shenzhen, China	Oct-Nov (Fall)	110	210*			Huang et al. (2012)
	Shanghai, China	Dec (Winter)		200	2-8	50-300	Gong et al. (2016)
	Texas, US	Sep (Fall)		170		20(@Dc=200 nm)	Schwarz et al. (2008)
	Beijing, China	Nov-Dec (Winter)		195-211	2.5		Liu et al. (2019)
		May-June (Summer)		185	1.4		
	Beijing, China	winter		209			Wu et al. (2021)
		summer		167			
Rural emission (RE)	Shenzhen, China	Nov (Fall)	120	222			Huang et al. (2012)
	This study	Dec (Winter)	122	213	1.6 (@Dc=180 nm)	52.4 (@Dc=180 nm)	
Biomass burning (BB)	Laboratory			189	1.2-1.4(@Dc=200 nm)		Pan et al. (2017)
	Texas, US	Sep (Fall)	140	210*		65(@Dc=200 nm)	Schwarz et al. (2008)
Remote ocean (RO)	Finnish Arctic	Dec-Jan (winter)		194	2.0(@Dc=150~200 nm)		Raatikainen et al. (2015)
Background	Paris, FR	Jan (Winter)		200		76(@Dc=200 nm)	Labrode et al. (2013)
Continent (BC)	Texas, US	Sep (Fall)				48(@Dc=200nm)	Schwarz et al. (2008)

*The density of rBC is 2 g cm⁻³

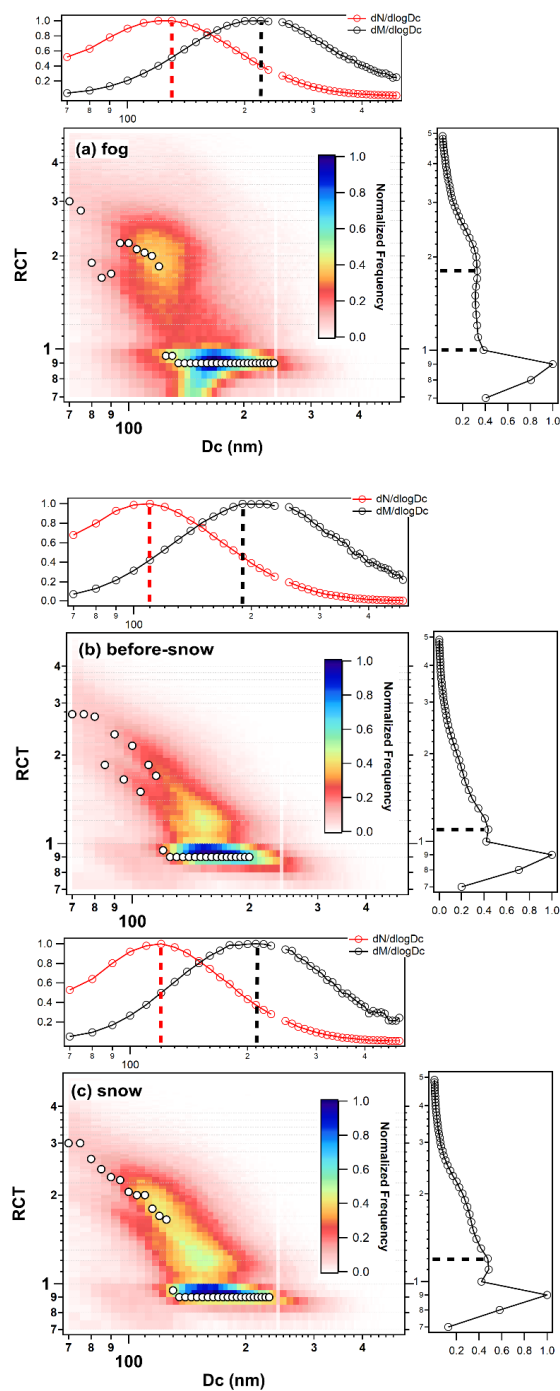


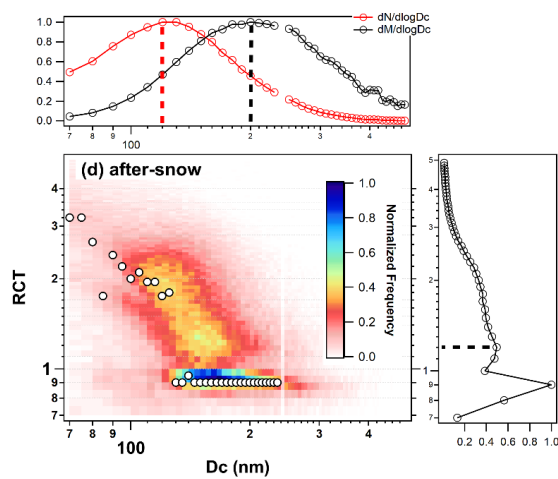
826

Table 2. Comparisons of E_{abs} in various field studies.

Method	Location	Time	E_{abs} (λ , nm)	Reference
TD+PAX+HR-AMS+AE33	Gucheng, China (rural)	Dec 2019–Jan 2020	1.32 ± 0.15 (870)	(Sun et al., 2021)
TD+PAX+SP2+AMS	California, USA (urban)	Jan–Feb 2013	1.21 ± 0.09 (870)	(Zhang et al., 2016)
SP2+CPMA+DMA	Beijing, China (Urban)	May–June 2018	1.15 (550)	(Liu et al., 2020)
SP2+PAX+ACSM	Xi'an, China (urban)	Dec 2012–Jan 2013	1.8 (870)	(Wang et al., 2014)
AE33+ACSM+OC/EC	Paris, France (suburban)	Mar 2014–Mar 2017	1.53 ± 0.93 (880)	(Zhang et al., 2018a)
TD+BBCES+IS	Shouxian, China (rural)	Jun–Jul 2016	2.3 ± 0.9 (532)	(Xu et al., 2018)
AFD	Yuncheng, China (rural)	Jun–Jul 2014	2.25 ± 0.55 (678)	(Cui et al., 2016)
SP2	Gucheng, China (rural)	Dec 2019	1.33 ± 0.57 (880)	This work

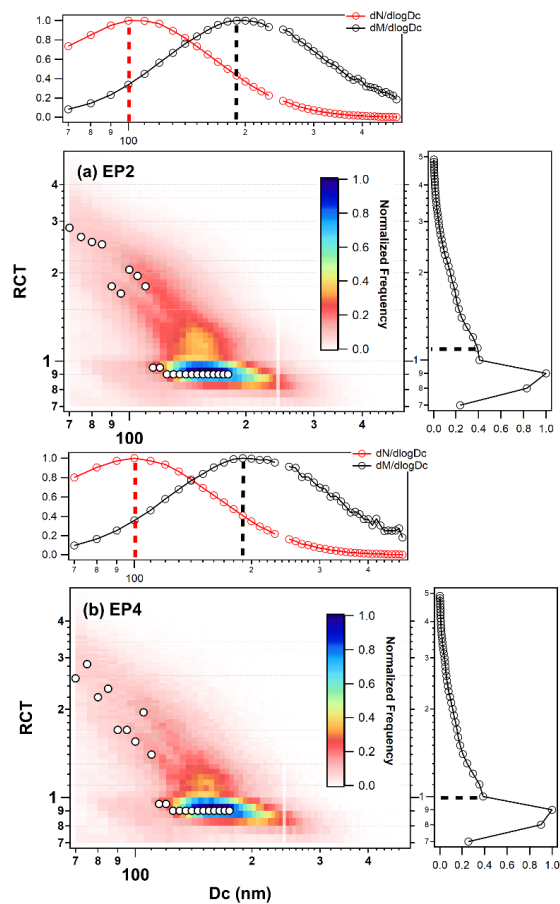
827





830

Figure 5: The RCT as a function of the *r*BC core diameter during (a) fog, (b) before-snow, (c) snow, and (d) after-snow events. The image plot is a 2D histogram, with the color denoting the normalized frequency in each bin. The right panel denotes the normalized (maximum=1) histogram of RCTs. The upper panel illustrates the number and mass size distribution of the *r*BC core.



835

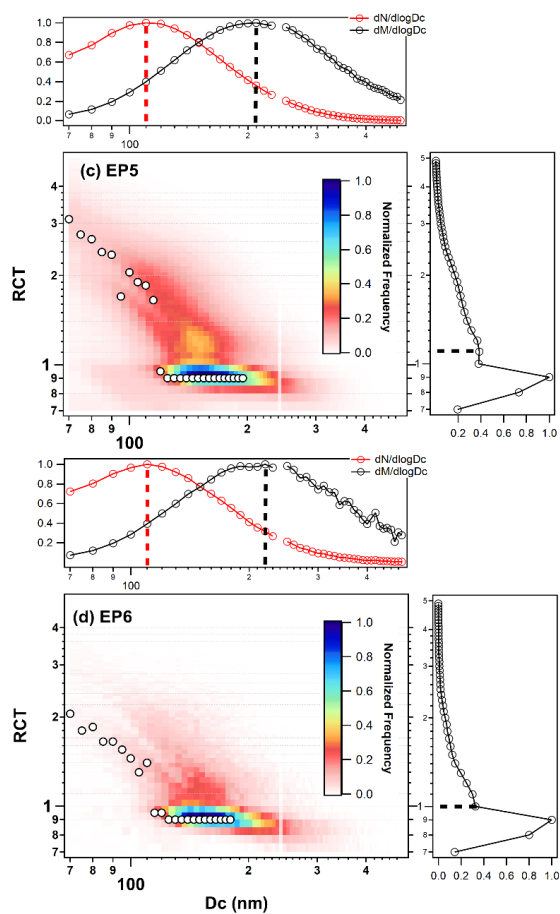


Figure 6: The RCT as a function of the *r*BC core diameter during (a) EP2, (b) EP4, (c) EP5, and (d) EP6 events. The image plot is a 2D histogram, with the color denoting the normalized frequency in each bin. The right panel denotes the normalized (maximum=1) histogram of RCTs. The upper panel illustrates the number and mass size distribution of the *r*BC core.

840

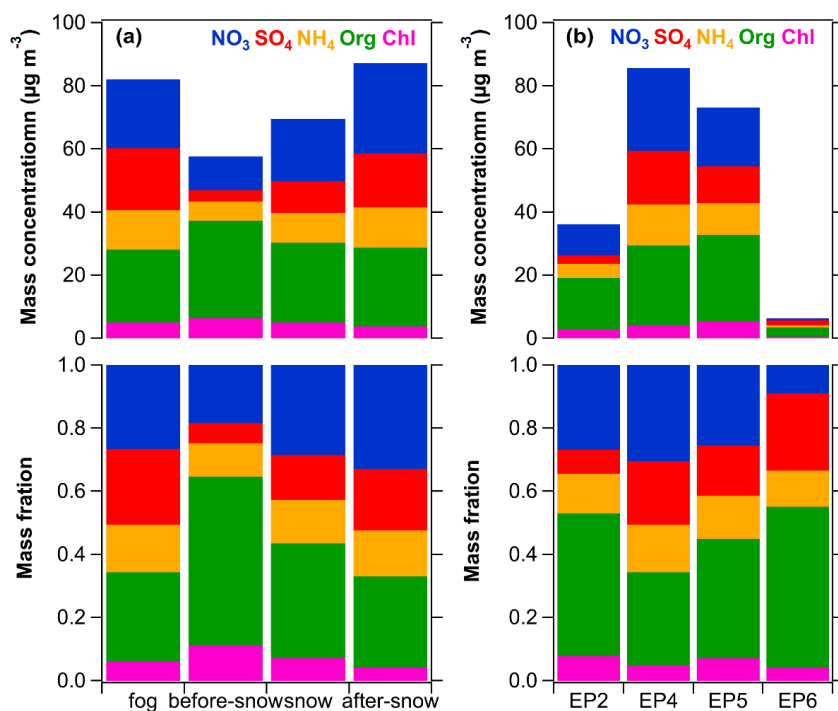
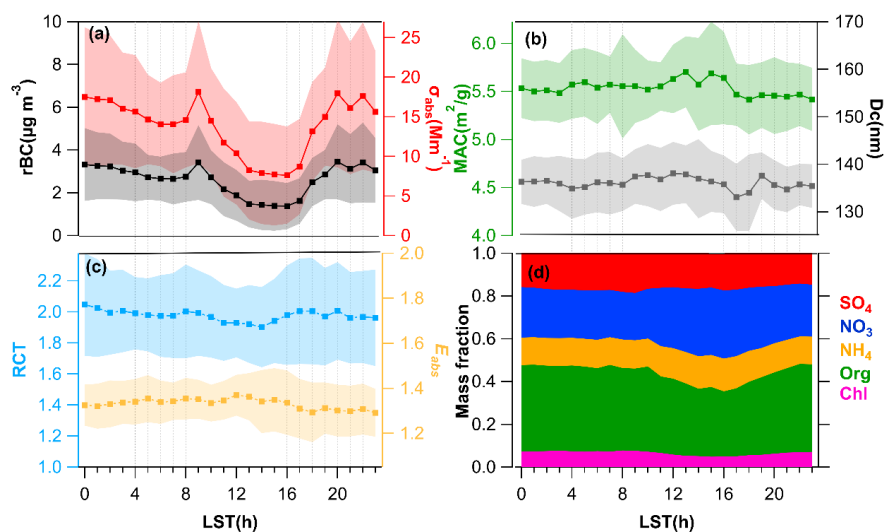
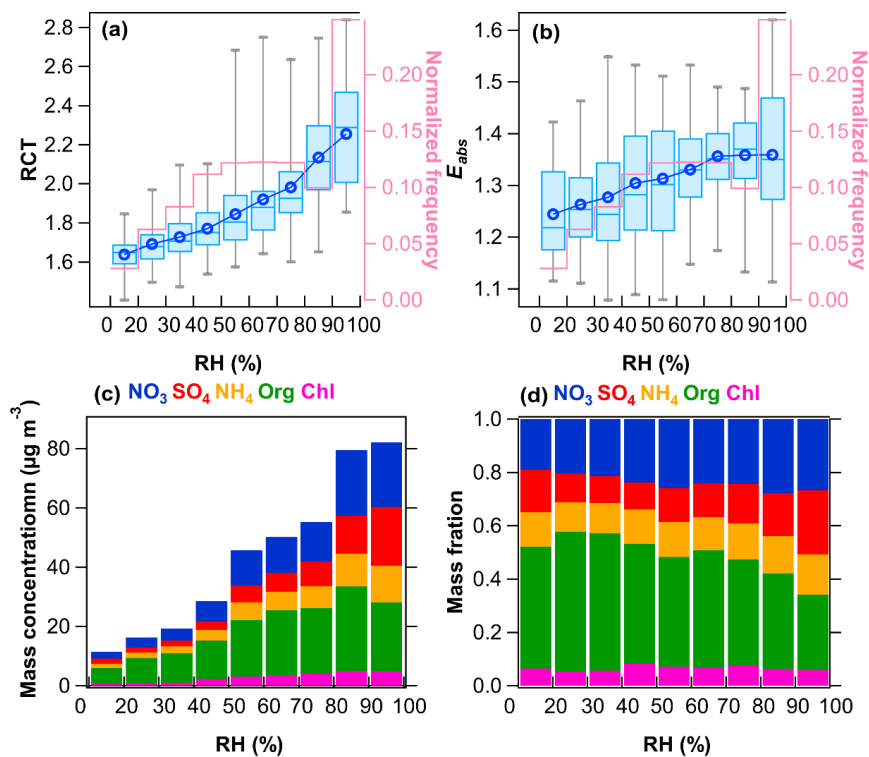


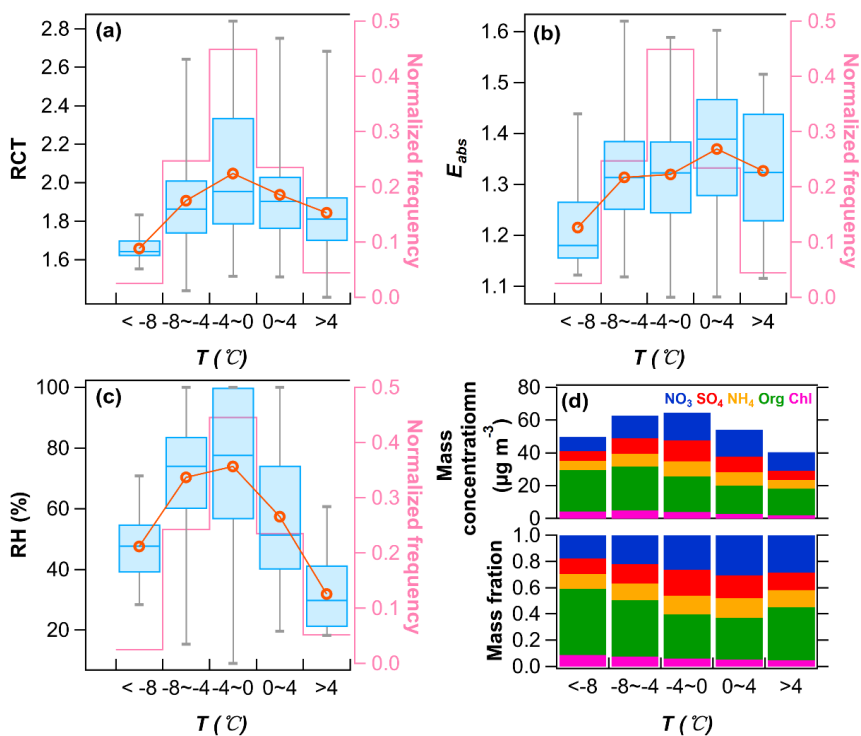
Figure 7: Changes in mass concentration and mass fractions of aerosol species during different periods.



845 Figure 8: Diurnal variation in (a) $r\text{BC}$ mass loading and absorption coefficients (σ_{abs}) of $r\text{BC}$ -containing particles, (b) the mass absorption cross-section (MAC) of $r\text{BC}$ -containing particles and the MMD, (c) relative coating thickness and absorption enhancement (E_{abs}) of $r\text{BC}$. The shaded area denote the standard deviation. (d) Mass fraction of aerosol species.



850 Figure 9: (a–b) RCT, E_{abs} dependency on RH. Blue circles represent the average values. The line inside the box indicates the median. The upper and lower boundaries of the box represent the 75th and 25th percentiles; the whiskers above and below each box represent the max and min values. The pink lines represent the normalized frequency of data points in each bin. (c–d) Mass concentration and mass fractions of aerosol species dependency on RH.



855

Figure 10: (a–c) RCT, E_{abs} , RH dependency on temperature. Red circles represent the average values. The line inside the box indicates the median. The upper and lower boundaries of the box represent the 75th and the 25th percentiles; the whiskers above and below each box represent the max and min values. The pink lines represent the normalized frequency of data points in each bin. (d) Mass concentration and mass fractions of aerosol species dependency on temperature.

860